

---

# Simultaneous identification of models and parameters of scientific simulators

---

**Cornelius Schröder**

University of Tübingen  
cornelius.schroeder@uni-tuebingen.de

**Jakob H. Macke**

University of Tübingen  
jakob.macke@uni-tuebingen.de

## Abstract

Many scientific models are composed of multiple discrete components, and scientists often make heuristic decisions about which components to include. Bayesian inference provides a mathematical framework for systematically selecting model components, but defining prior distributions over model components and developing associated inference schemes has been challenging. We approach this problem in an amortized simulation-based inference framework: We define implicit model priors over a fixed set of candidate components and train neural networks to infer joint probability distributions over both, model components and associated parameters from simulations. To represent distributions over model components, we introduce a conditional mixture of multivariate binary distributions in the Grassmann formalism. Our approach can be applied to any compositional stochastic simulator without requiring access to likelihood evaluations. We first illustrate our method on a simple time series model with redundant components and show that it can retrieve joint posterior distribution over a set of symbolic expressions and their parameters while accurately capturing redundancy with strongly correlated posteriors. We then apply our approach to drift-diffusion models, a commonly used model class in cognitive neuroscience. After validating the method on synthetic data, we show that our approach explains experimental data as well as previous methods, but that our fully probabilistic approach can help to discover multiple data-consistent model configurations, as well as reveal non-identifiable model components and parameters. Our method provides a powerful tool for data-driven scientific inquiry which will allow scientists to systematically identify essential model components and make uncertainty-informed modelling decisions.

## 1 Introduction

Computational models are a powerful tool to condense scientific knowledge into mathematical equations. These equations can be used for interpreting and explaining empirically observed phenomena and predicting future observations. Scientific progress has always been driven by competing models, dating back to disputes about the heliocentric system [1]. However, newly developed models are rarely that disruptive; instead, they are often created by combining existing components into larger models. For example, the original SIR model [2] describes the dynamics of infectious diseases by three population classes (susceptible, infective, recovered), but was later expanded to include further epidemiological classes (e.g., temporary immune groups [3]). Similar modularity can be found, for example, in computational neuroscience models: The original Hodgkin-Huxley model [4] for the dynamics of action potentials consisted of only two voltage-gated ion channels ( $K^+$ ,  $Na^+$ ), but more recent models [5, 6] are based on compositions of a myriad of different channels [7]. Similarly, there exist many different variants of drift-diffusion models (DDM) [8] in cognitive neuroscience: All of them follow the basic concept of modelling the decision process by a particle following a stochastic differential equation and eventually hitting a decision-boundary. There are many possible choices of

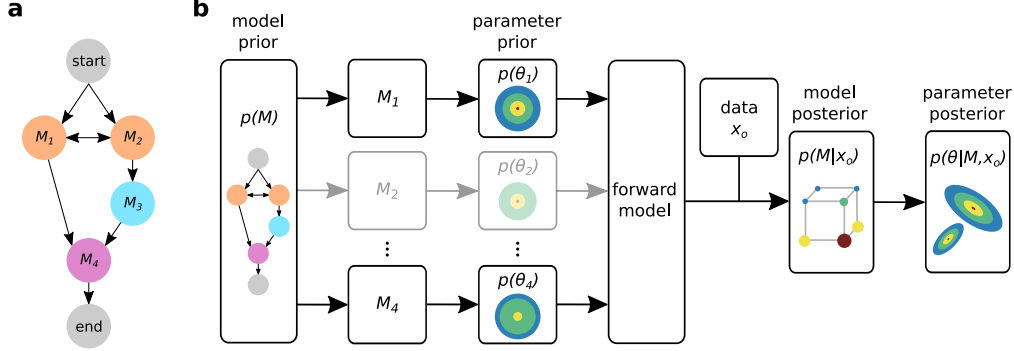


Figure 1: **Simulation-based model inference (SBMI) scheme.** (a) The model prior  $p(M)$  is given implicitly by a graph. A random walk from the *start* to the *end* node corresponds to a draw from this prior. (b) We first sample from the model prior and the corresponding parameter priors  $p(\theta_i)$  to compile a forward model. Following this sampling procedure, we generate training data with which we can learn an approximation of the joint posterior  $p(M, \theta|x_o)$  given some observed data  $x_o$  by factorizing the posterior into  $p(M|x_o)p(\theta|M, x_o)$ .

noise models, drift dependencies, and boundary conditions. This rich model class and many of the different components have been extensively studied on a wide range of experimental measurements [9–15].

How can one automatically infer such models from data, including *both* the compositions of components and the associated parameters? One challenge is posed by the fact that, for many such models, evaluating the likelihood function is not tractable, rendering standard likelihood-based approaches inapplicable. Approximate Bayesian computation (ABC) [16], offers a framework to deal with this challenge in a systematic way, and in the last years, the development of new methods has been fueled by advances in neural network-based density estimation [17] leading to new simulation-based inference (SBI) methods [18–20]. SBI has been successfully applied to various fields like astronomy [21], robotics [22], neuroscience [23–25] and cognitive science [26, 27].

However, in addition to inferring parameters, we also need to be able to compare and select models comprised of different components to select between competing theories. Standard methods for Bayesian model comparison (or selection) rely on the *Bayes factor* [28], i.e. the ratio of model evidence for two different models  $M_1$  and  $M_2$ :  $B_{12} := p(x_o|M_1)/p(x_o|M_2)$ . Multiple approaches have been developed for estimating Bayes factors, most of which are based on (rejection) sampling [29] and are computationally expensive. Alternative approaches include approximating the model evidence by applying harmonic mean estimators to emulators of the likelihood function [30], or by directly targeting the model posteriors in an amortized manner [31, 32]. While these methods infer the model evidence separately for each model or assume a fixed set of models to compare, our approach allows for a comparison of flexible combinations of model components in a fully amortized manner.

*Symbolic regression* approaches aim to learn interpretable mathematical equations from observations—while this might seem like a conceptually very different problem, it is methodologically related, as one can also interpret mathematical equations as being composed of different model components. Inferring symbolic equations from data can be tackled by genetic programming [33, 34], by performing sparse regression over a large set of base expressions [35, 36] or by using graph neural networks [37]. Alternatively, symbolic regression has been approached by designing neural networks with specific activation functions [38, 39], optimizing these networks with sparsity priors [40] and using Laplace approximations to infer uncertainties over their weights [41]. Building on the success of transformers, [42] introduced a transformer-based approach for symbolic regression, which was recently extended to capture differential equations [43].

Our work builds on these advances in both SBI and symbolic regression. However, our goal is to infer *joint* posterior distributions over a set of different model components, *as well as* over their associated parameters. One can interpret our approach as performing fully probabilistic symbolic regression not on ‘atomic’ symbols, but rather on expression ‘molecules’ which are provided by domain experts

and represent different mechanisms that might explain the observed data. As we will show, accurate inference of joint posteriors is crucial for obtaining interpretable results in the presence of redundant model components: A common situation in scientific applications is that different components are functionally similar (e.g., ion channels with similar dynamics [7]), resulting in explaining-away effects and strongly correlated posterior distributions. Hence, inference methods need to be able to accurately handle such settings to obtain scientifically interpretable results. We address this challenge by providing a network architecture for joint inference, which includes a flexible representation over model components using mixtures of multivariate binary distributions in the Grassmann formalism [44]. Second, for such a procedure to be able to provide parsimonious results, the ability to flexibly specify priors over models is crucially important. Our procedure only requires the ability to generate samples from the prior (like [42]), without requiring access to evaluations of prior probabilities. Third, our approach is fully *amortized*: Once the inference network has been trained, approximate posteriors over both model components and parameters can be inferred almost instantly, without any computationally expensive MCMC sampling and/or post-hoc optimizations at inference-time.

In the following, we first describe our inference method (Section 2) and showcase it on an additive model related to symbolic regression (Section 3.1). We then apply it to DDMs and experimental decision-making data (Section 3.2) and show that it can successfully retrieve interpretable posteriors over models.

## 2 Method

Our proposed method, *simulation-based model-inference* (SBMI), performs inference over a model  $M$  consisting of different model components  $M_i$  and their associated parameters  $\theta_i$ . More specifically, we use a neural posterior estimation (NPE) method to approximate a joint posterior distribution  $p(M, \theta|x_o) = p(M|x_o)p(\theta|M, x_o)$  given some observed data  $x_o$  end-to-end (Fig. 1). We assume that we have a ‘black-box’ model from which we can draw samples  $x_j \sim p(x|M, \theta)$ , but don’t necessarily have access to the likelihood, any other internal states, or gradients of the model. Approximate Bayesian inference is performed by first generating simulations which are then used to learn posterior distributions. These can be evaluated in an amortized manner for new observations  $x_o$  to get the full joint posterior  $p(M, \theta|x_o)$ .

### 2.1 Priors and data generation

To allow maximal flexibility in designing appropriate priors, SBMI only requires access to an implicit prior distribution from which we can sample models. We here define the model prior by a directed graph, in which the vertices correspond to model components  $\{M_i\}_{i \in \{1, \dots, N\}}$ , and each edge holds a weight (Fig. 1a). To sample from the prior, we perform a random walk on the graph and represent each model  $M = (M_1, \dots, M_N)$  as an ordered binary vector of length  $N$ . By changing the edge weights we can encode additional prior knowledge, for example, to favour simple models over complex models, or to encourage (or discourage) the co-occurrence of specific model components. This graph representation gives us the possibility to flexibly encode prior knowledge of the model by carefully defining its structure and weights with the help of domain expertise.

Once we have sampled a model  $M$ , we define the prior of the corresponding model parameters as the product of the component-specific priors:  $p(\theta|M) = \prod_{i|M_i=1} p(\theta_i)$ , i.e. the parameter vector  $\theta$  is of variable size and matches a specific model  $M$ . The component-specific priors  $p(\theta_i)$  can correspond to any continuous, potentially multivariate, distribution.

To generate training data for learning an approximation of  $p(M, \theta|x_o)$  we need a ‘compiler’ that turns the model representation  $(M, \theta)$  into a simulator which then generates synthetic data  $x$ . These

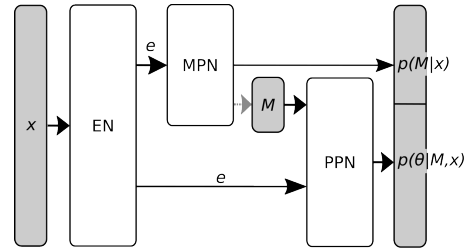


Figure 2: **SBMI network architecture.** Data  $x$  is passed through an embedding net (EN). The embedded data  $e$  is forwarded to the model posterior network (MPN), which learns posteriors over different model components, and the parameter posterior network (PPN) which learns the posterior distributions over parameters given specific models  $M$ . Gray boxes correspond to network inputs / outputs.

compilers and simulators will generally be specific to the model type and based on domain-specific toolboxes. In our numerical experiments, we built a flexible interface to symbolic calculations based on *SymPy* [45] for the additive model (Sec.3.1), and the *PyDDM* toolbox [46] for the drift-diffusion model (Sec. 3.2).

## 2.2 Inference

We want to perform inference over the joint posterior distribution  $p(M, \theta|x)$  of the model and its parameters, given some data  $x$ . We can factorize this distribution  $p(M, \theta|x) = p(M|x)p(\theta|M, x)$  and approximate it by learning jointly two coupled network modules (Fig. 2): The first module learns an approximation to the model posterior  $q_\psi(M|x) \approx p(M|x)$  and the second one an approximation to the parameter posterior  $q_\phi(\theta|M, x) \approx p(\theta|M, x)$  conditioned on the data and the model. As the data  $x$  might be high-dimensional (or, in principle, of variable length [42, 27]) we use an additional embedding net to project it to a low-dimensional representation before passing it to the posterior networks.

**Model posterior network** To approximate the multivariate model posterior  $p(M|x)$  we introduce mixture of multivariate binary Grassmann distributions (MoGr). Multivariate binary Grassmann distributions were recently defined by Arai [44], and allow for analytical probability evaluations. Additionally, closed-form expressions for marginal and conditional distributions are available, which in turn can be directly used for efficient sampling. An  $n$ -dimensional binary Grassmann distribution  $\mathcal{G}$  on  $Y = (Y_1, \dots, Y_n)$  is parameterized by a  $n \times n$  matrix  $\Sigma$  which is analogous to the covariance of a normal distribution, but not necessarily symmetric. The mean of the marginal distribution is represented on the diagonal and the covariance is the product of the off-diagonal elements [44]:

$$\mathbb{E}[Y_i] = \Sigma_{ii}, \quad \text{Cov}[Y_i, Y_j] = -\Sigma_{ij}\Sigma_{ji}.$$

We define further a mixture of Grassmann distribution as  $\text{MoGr}(Y) = \sum_i \alpha_i \mathcal{G}_i(Y)$  for a finite partition  $\sum_i \alpha_i = 1$  and Grassmann distributions  $\mathcal{G}_i$ . We denote the corresponding conditional distribution by  $\text{MoGr}(Y|e) = \sum_i \alpha_i \mathcal{G}_i(Y|e)$ , for some real-valued context vector  $e$  (which will be the embedded data in our case). Further details (including restrictions on  $\Sigma$ , some key properties, and implementation details) in Appendix A2. We trained the model posterior  $p(M|x)$  represented as conditional MoGr distribution  $\text{MoGr}(M|x) \approx q_\psi(M|x)$  by minimizing the negative log-likelihood. The model loss  $\mathcal{L}_M$  is therefore defined by  $\mathcal{L}_M(\psi) = -\log q_\psi(M|x)$ .

**Parameter posterior network** The parameter posterior network  $q_\phi(\theta|M, x)$  needs the flexibility to deal with different dimensionalities, as  $\theta$  is only defined for included model components ( $M_i = 1$ ). While recent SBI approaches typically used normalizing flows [17] for parameter inference, we use a mixture density network (MDN) of Gaussian distributions on the full-dimensional parameter space (with dimension  $n = \sum_i \dim(\theta_i)$ ) and marginalize out the non-enclosed model components, allowing the network to learn dependencies across model components (which is critical, e.g., to account for compensation effects between redundant components).

We construct this flexible MDN by defining for every  $\theta$  its complement  $\theta^C$  as the parameter dimensions not present in  $\theta$  and  $\bar{\theta} = (\theta, \theta^C)$ . We further define  $\bar{p}$  as the  $n$ -dimensional distribution acting on  $\bar{\theta}$ . We can now define the parameter posterior network  $q_\phi(\theta|M, x)$  by marginalizing out  $\theta^C$ ,

$$q_\phi(\theta|M, x) = \int \bar{p}(\bar{\theta}|M, x) d\theta^C.$$

We use the standard NPE loss [19] for the parameter posterior network  $\mathcal{L}_\theta$ :  $\mathcal{L}_\theta(\phi) = -\log q_\phi(\theta|M, x)$ . The final loss function for the training of the three different network modules (embedding net, model, and parameter posterior network) is then defined as the expected sum of the two posterior losses:  $\mathcal{L}(\psi, \phi) = \frac{1}{\#L} \sum_l \mathcal{L}_{M_l}(\psi) + \mathcal{L}_{\theta_l}(\phi)$ , for a batch of training samples  $\{(\theta_l, M_l, x_l)\}_{l \in L}$ . See Algorithm 1 for pseudocode. For a fixed embedding net with output  $e(x)$  both posterior networks  $q_\psi(M|e(x))$  and  $q_\phi(\theta|M, e(x))$  converge to an optimum of  $\mathcal{L}_M$  and  $\mathcal{L}_\theta$  respectively. Our implementation is based on the *sbi* toolbox [47] (details in Appendix A4).

**Local and global uncertainties:** SBMI allows us to calculate two different uncertainties for the posterior predictives, depending on whether uncertainty about model-choice is taken into account or

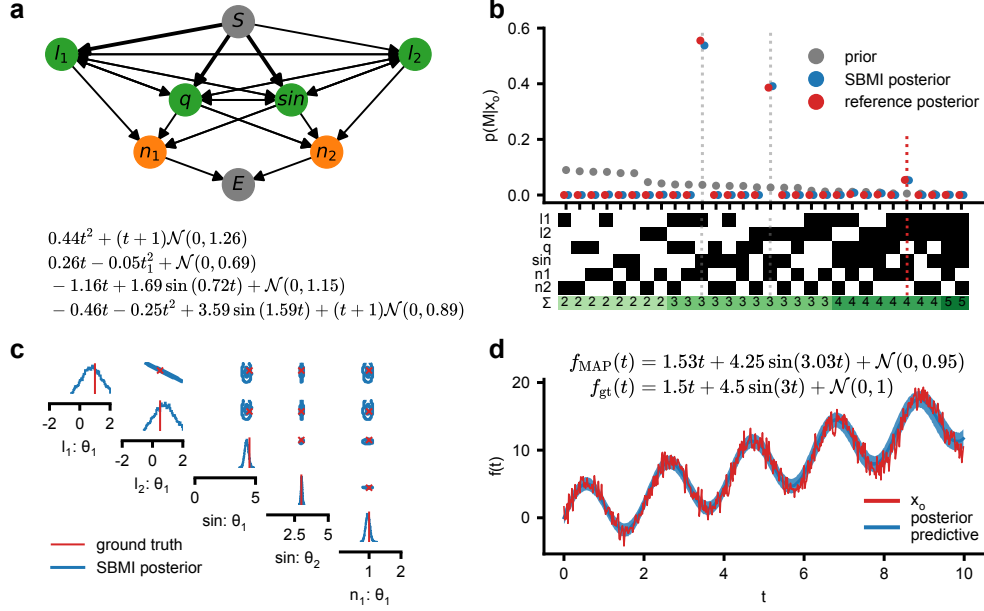


Figure 3: **Illustration on Additive Model.** (a) Model prior represented as graph, the width of the edges corresponds to their initial weights, which can change dynamically. A random walk from *start* ( $S$ ) to *end* node ( $E$ ) corresponds to one draw from the prior. Four prior samples are shown. (b) Empirical prior distribution, reference and SBMI posterior distribution for one example observation, generated by the model highlighted by the red dashed line. The model vectors are shown as binary image. SBMI accurately recovers the posterior over model components. Marginal distributions in Fig. S2. (c) One- and two-dimensional marginals of the parameter posterior inferred with SBMI, conditioned on the ‘true model’ (red dotted line in (b)). Note the strongly negatively correlated (degenerate) posterior between the redundant model components  $l_1$  and  $l_2$ . Parameter posteriors for additional models in Fig. S2. (d) Predictive samples on an observation  $x_o$  from  $f_{\text{gt}}$ . Blue: Mean  $\pm$  std. as local uncertainties of the posterior predictives  $x \sim p(x|\theta, M)$  with  $\theta \sim p(\theta|M, x_o)$ .

not: *Local* uncertainties [41] are defined as the uncertainty of parameter posteriors conditioned on a specific model  $M_i$ :  $x \sim p(x|M_i, \theta)$  with  $\theta \sim p(\theta|M_i, x_o)$ . In contrast, for the *global* uncertainty, the joint posterior is taken into account:  $x \sim p(x|M, \theta)$  with  $M, \theta \sim p(M, \theta|x_o)$ .

### 3 Experiments

We demonstrate SBMI on two model classes: An illustration on an additive model of a one-dimensional function  $f(t)$  and variants of *drift diffusion models* (DDMs) from cognitive science.

#### 3.1 Additive model

For the additive model, we used two linear, a quadratic, a sinusoidal, and two different noise terms (details in Table S1), all evaluated on an equidistant grid on the interval  $[0, 10]$ . These could be seen as the ‘base functions’ in a symbolic regression task. An example function with three model components is  $f(t) = \theta_1^1 t^2 + \theta_2^1 \sin(\theta_2^2 t) + \mathcal{N}(0, \theta_3^1)$ , for which the parameters  $\theta_i^j$  are drawn from the parameter priors  $p(\theta_i)$ . To investigate how SBMI fares in the presence of non-identifiability, we included two identical linear components which only differ in their prior probability. We defined the model prior as a dynamically changing graph (Fig. 3a) which favors simpler models (Fig. 3b). As embedding net, we used a CNN followed by fully connected layers (details in Appendix A6). We generated a dataset of 500k prior samples, of which 10% were used as validation data.

In the presented setup, we have access to the likelihood function  $p(x_o|M, \theta)$ , and can approximate the model evidence  $p(M|x_o) \approx \hat{p}_{\text{reference}}(M|x_o) \sim p(x_o|M)p(M)$  by sampling for each model

Table 1: **SBMI performance for the additive model.** Comparison of SBMI and reference model posteriors in terms of Kullback-Leibler divergence (KL) and marginal performances. We calculated reference posteriors for 100 observations  $x_o$  (see Table S1 for performances of individual components). For the RMSE we used 1k observations  $x_o$  and ‘Reference’ corresponds to the RMSE between the observations  $x_o$  and samples  $x$  under the ground truth model and parameters. We report mean and standard deviation.

Measure	Reference (Posterior)	SBMI Posterior	Prior
KL	-	0.28 (0.71)	11.26 (1.88)
Marginal Performance	0.88 (0.15)	0.86 (0.09)	0.53 (0.12)
RMSE	6.87 (6.05)	7.05 (6.19)	15.24 (7.95)

$M$  corresponding parameters  $\theta_i^j$  and evaluating the likelihood  $p(x_o|M)$  (details in Appendix A5). We call the resulting approximation *reference posterior*, and will use it to evaluate the accuracy of the posterior inferred by SBMI. As the parameter space for  $\theta$  can be high-dimensional, and the corresponding posterior distribution  $p(\theta|M, x_o)$  can be narrow, a reliable numerical approximation needs an extensive amount of samples and model evaluations for each of the model  $M$ .

Across 100 observations  $x_o$  for which we computed reference posteriors, the Kullback–Leibler divergence (KL) between the reference posterior and the SBMI posterior  $\text{KL}(\hat{p}_{\text{reference}}(M|x_o)||q_\psi(M|x_o))$  was, on average,  $0.28 \pm 0.71$  (mean  $\pm$  std.), which is much less than the KL between prior and posterior ( $11.26 \pm 1.88$ ). Additionally, we can compare samples from the model posterior to the ground truth model and evaluate whether we recovered the correct model components. The performance of the marginal model posterior distributions inferred by SBMI is very similar to that of the reference posteriors  $\hat{p}_{\text{reference}}(M_i|x_o)$  across 100 different test samples  $x_o$  (Table 1). We note that, in initial experiments in which we used masked autoregressive density estimators (MADE) [48] (instead of the Grasmann mixtures) exhibited worse performances in comparison (Fig. S1), indicating the power and flexibility of MoGr distributions.

For the evaluation of the joint posterior  $p(M, \theta|x_o)$ , we focused on the evaluation of the posterior predictives for 1k test observations  $x_o$ . We sampled models  $M_l \sim q_\psi(M|x_o)$  and associated parameters  $\theta_l \sim q_\phi(\theta|M_l, x_o)$  from the inferred posteriors and ran the forward model  $x_l \sim p(x|M_l, \theta_l)$ . Based on these simulations, we calculated the root-mean-squared-error (RMSE) of the simulations  $x_l$  to the observed data  $x_o$ . The average RMSE between posterior predictive samples and corresponding observations  $x_o$  for a test set of 1k observations is  $7.05 \pm 6.19$  (mean  $\pm$  std.), which is similar to the RMSE between the observations  $x_o$  and samples with the same ground truth parameters, and much smaller than the RMSE evaluated on prior samples (Table 1).

Next, we showcase SBMI for a specific example observation  $x_o$  in which the ground truth model has two linear, a sinusoidal, and a stationary noise component (Fig. 3b-d): The SBMI model posterior matches perfectly the reference posterior and predicts the linear components as expected, ordered by the prior probabilities (Fig. 3b). The parameter posterior obtained with SBMI and conditioned on the ground truth model accurately recovers the ground truth parameters (Fig. 3c). Accessing the joint posterior distribution enables us to first see the perfectly correlated parameter distribution for the slope parameter of the linear components. Second, we detect compensations mechanisms for a model which contains only one linear component: In this case, the predicted parameter for  $l_1$  is the sum of the ground truth parameters of  $l_1$  and  $l_2$ , resulting in the same functional expression (Fig. 3). For the posterior predictives (Fig. 3d) we see that most of the observed data  $x_o$  lies within an uncertainty bound of one standard deviation around the mean prediction. The local uncertainties overlap perfectly in this case, as all models with non-negligible posterior mass have the same expressional form. With the inferred model posterior we can easily compute the Bayes factors via  $\frac{p(M_1|x_o)}{p(M_2|x_o)} \frac{p(M_2)}{p(M_1)}$  to compare different models on an observation  $x_o$ . In this example, we get Bayes factors of  $B_{l_1 l_2} = 1.02$  for the comparison of the two models with a single linear component, and  $B_{l_1 l_{12}} = 1.45$ , if we compare the model with component  $l_1$  with the one in which both model components are present. Following the scale by [49] this would be ‘inconclusive’ about the preference of the models.

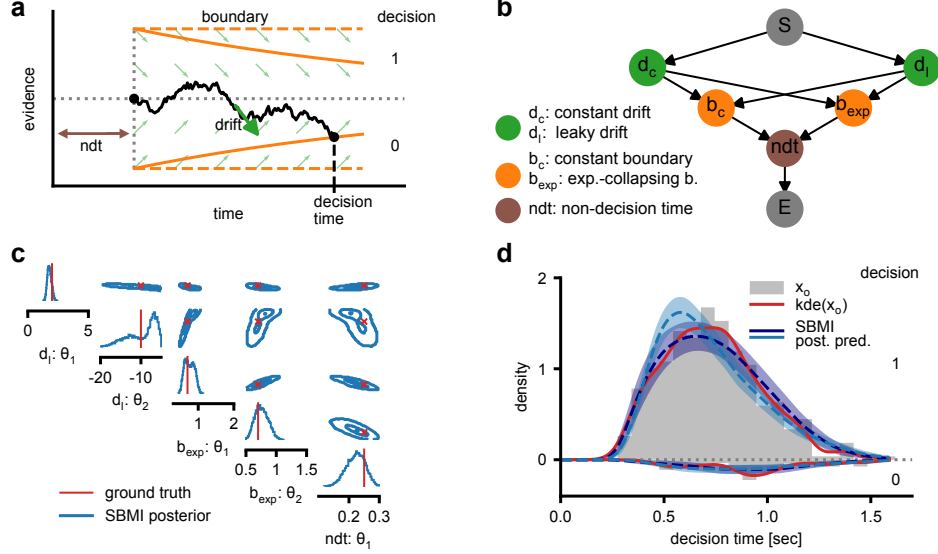


Figure 4: **SBMI on Drift-Diffusion Models.** (a) A decision process is modelled by a one-dimensional stochastic process. A binary decision is taken once the process hits the upper or lower boundary, resulting in a two-dimensional output (a continuous decision time and a binary decision). (b) The model prior is a graph consisting of two drift ( $d_c$ ,  $d_l$ ) and two boundary ( $b_c$ ,  $b_{exp}$ ) components, as well as a non-decision time ( $ndt$ ). (c) An example parameter posterior inferred with SBMI. Here, both the ground truth model and the predicted model, have leaky drift and exponentially collapsing boundary conditions. (d) Posterior predictives with local uncertainties as mean  $\pm$  std. for the two most likely models (dark blue with  $q_\psi(M|x_o) = 0.75$  and light blue with  $q_\psi(M|x_o) = 0.25$ ).

### 3.2 Drift-Diffusion model

After this illustrative example (in which we were able to compare SBMI with a reference posterior), we turn to DMMs, a scientific model class that we will apply to experimental data: DDMs can be described by a stochastic differential equation for a decision variable  $z$ :  $dz = d(z, t)dt + dW$ , with initial condition  $z_0$ , drift term  $d$ , and a Wiener noise process  $W$ . A decision is taken when the decision variable hits the boundary  $|d(z, t)| \geq b(t)$  (Fig. 4a). An additional parameter delays the starting time of the process (‘non-decision time’). We included two different drift terms (constant and leaky), two boundary conditions (constant and exponentially collapsing), and the non-decision time to our prior (Fig. 4b, details in Appendix A6.2), resulting in a highly flexible model class. Similar models have previously been applied successfully to experimental data [46].

Training data was generated with the *pyDDM* toolbox [46]. For each  $\theta$  we sampled 400 independently identically distributed (iid) trials, resulting in a  $400 \times 2$  data matrix of continuous decision times and binary decisions. Initial experiments showed that models with leaky drift and constant boundary conditions often resulted in unrealistically long decision times ( $>10$ sec), and we therefore discouraged their co-occurrence by including a negative coupling between these two terms in the model prior. We used a permutation invariant embedding network, previously used on iid trial data [50, 26]. In this setup, the single-trial data is first processed by a fully connected network, mean pooled, and then passed through additional fully connected layers (details in Appendix A6).

For the DDM setup we don’t have efficient access to the likelihood and therefore can not compute reference posteriors. To still evaluate the performance of SBMI, we focus on the evaluation of model posteriors and predictive performances for a test set of 1k data points. The average marginal performance of the model posterior for the drift and boundary components is  $0.87 \pm 0.21$  (std.) (see Table S3 for individual performances). For about 40% of the test data we get highly certain model posteriors with  $p(M|x_o) > 0.99$ , indicating that model identifiability is dependent on the observed data.

To measure the performance of the posterior predictives, we compared the mean decision times, the standard deviation of the decision times, as well as the number of correct trials to the observed data  $x_o$ . Additionally, we used the mean-squared error (MSE) on the weighted density functions of the two different decisions, similar to [46]. The different measures on the posterior predictives for the test data are close to their lower bounds (see Table 2), calculated on trials resampled from a model with the ground truth parameter. This suggests that, even for non-identifiable models, the SBMI inferred posterior predictives are close to data from the ground truth model.

For an example observation  $x_o$  from a model with a leaky drift component and exponential collapsing boundaries, the 'true' model has a posterior probability of 0.75 and a model with a constant drift instead has a posterior probability of 0.25, resulting in a Bayes factor of  $B = 2.32$ , or a 'barely worth mentioning' difference [49]. For the 'true' model the ground truth parameters lie in regions of high parameter posterior mass, with some uncertainty, especially in the leak parameter  $\theta_2$  of the drift component (Fig. 4 c). The posterior predictives match the data well if conditioned on the 'true' model. For the model with the constant drift term, we see a slight skew to earlier decision times, compared to the model with leaky drift (Fig. 4 d). If we inspect the global uncertainties (Fig. S3) we see a good correspondence for the global uncertainties, also reflected in the MSE losses (scaled by  $10^2$ ): For trials resampled with the ground truth parameters we find an MSE of  $0.57 \pm 0.13$  which matches the MSE of the first model ( $0.58 \pm 0.14$ ) and the second model is only slightly worse ( $0.61 \pm 0.14$ ). Further inspecting the posterior distributions shows that the model with the constant drift term exhibits shorter non-decision times, larger initial boundaries and faster collapsing boundaries (Table S5). Interpreting the inferred values model-independent as behavioral variables can therefore be difficult, as different models might lead to different inferred values.

**DDM on experimental data** To demonstrate SBMI on empirical data, we used a published dataset of perceptual decision-making data from monkeys [51] performing a random dot motion discrimination task. Moving dots with different coherence rates (0, 3.2, 6.4, and 12.8%) were visually presented and animals had to identify the direction of movement (Appendix A6.2).

When we used the trained posterior network to perform amortized inference on the different experimental conditions of the experimental data, the model posterior is certain about the leaky drift and exponentially collapsing boundary component with  $p(M|x_o) \approx 1$  for all coherence rates. For all measures on the posterior predictives we found similar mean performances for the SBMI inferred models compared to point estimates (Table S6). But, as expected, the MSE had higher variances in the different experimental conditions compared to the variance of multiple point estimates (data not shown). This can also be seen in the decision time densities of the posterior predictives for which the experimental data lies within the uncertainty bounds (Fig. 5),

whereas the predictives of the point estimates from *pyDDM* are not distinguishable. However, when we look at the actual parameters, we see that different point estimates are spread out for some of the parameters, and all lie in regions of high SBMI parameter posterior mass. An example of the two-dimensional marginals for the coherence of 6.4% is shown in Figure S4.

## 4 Discussion

We presented SBMI, a method for inferring joint posterior distributions over both model components of scientific simulators and their associated parameters end-to-end. For the model inference network of SBMI, we used a mixture of conditional multivariate binary Grassmann distributions to flexibly and efficiently approximate posterior distribution over models. To deal with the variable dimensionality of

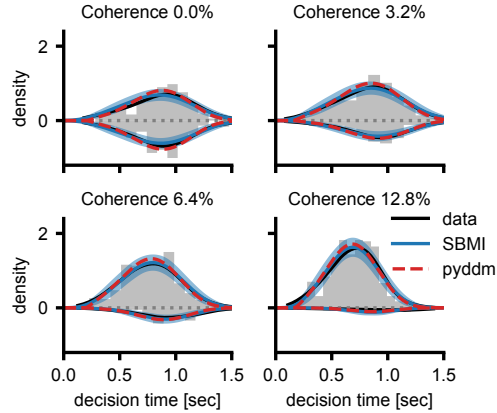


Figure 5: **SBMI on experimental data.** Experimental data with histograms (grey), mean posterior predictives  $\pm 2$ std. and *pyDDM* fits for different coherence rates.



Table 2: **DDM posterior predictive performance.** Comparison of mean decision times  $\mu$  and standard deviation of decision times  $\sigma$  of the ground truth data ( $\cdot$ ) to posterior predictive samples. The lower bound is based on resampling 400 trials with the same ground truth parameters as the observation  $x_o$ . We report the mean and standard deviation (in brackets) for the different measures based on 1k test datapoints.

Measure	Lower bound	Posterior
decision time: $ \mu - \hat{\mu} $	0.03 (0.04)	0.08 (0.21)
decision time: $ \sigma - \hat{\sigma} $	0.21 (0.27)	0.26 (0.35)
deviation correct trials in %	1.10 (1.37)	1.56 (2.64)
MSE on densities ( $\cdot 10^{-2}$ )	3.14 (5.83)	3.23 (6.57)

the parameter posterior, we used a Mixture Density Network which allows efficient marginalization over absent model components. While marginalization of MDNs has recently been used to investigate the influence of summary features in NLE *post-hoc* [52], we here used marginalization during training time. By inferring the joint posterior distribution over models and parameters, SBMI allows us to learn parameter dependencies between model components and compensatory mechanisms, in a fully amortized way.

We showcased our method on an additive model and showed that posteriors retrieved by SBMI are in very close agreement with reference posteriors, indicating the accuracy of its inferences. In addition, we showed that SBMI returns parameter posteriors which recover the ground truth parameters and that it can handle strongly correlated parameter distributions and compensation mechanisms between different model components. Applying our method to DMMs, a real scientific model from cognitive science, shows that different metrics for the posterior predictives are all near performance bounds. An in-depth analysis of the parameter posteriors identifies compensatory mechanisms for some parameters (such as the non-decision time), and showcases the importance of a ‘model-aware’ interpretation of parameter posteriors, which is straightforward in SBMI. On experimental data, SBMI automatically retrieves a model which was previously suggested by scientists to be well suited for the used dataset [46], and which outperforms simpler DDM-versions.

Like other SBI methods, SBMI gives a full parameter posterior which allows us to investigate parameter degeneracy and draw conclusions in an uncertainty-aware manner. But additionally, SBMI infers the uncertainty related to the model choice itself and potential interactions between the parameters of different model components. In the symbolic regression framework a similar perspective was presented [41] who estimated local uncertainties by Laplace approximations of the inferred network representations for individual equations, and used a fixed number of equations for the global uncertainty. While this gives some measure of uncertainty, SBMI is able to recover the *full* posterior and its associated uncertainty.

SBMI enables us to compare different model compositions in a fully amortized manner, allowing one to test and compare a large set of and competing theories without the need to exhaustively infer each possible combination individually for separate comparisons based on Bayes-factors. Additionally, the amortized nature of SBMI makes it very easy to check how robust posteriors over models are when observations change. Similarly, amortization also makes it straightforward to perform additional coverage and calibration tests [53, 54], a potential avenue for future work.

For real-world applications the success of SBI also relies on appropriate prior choices [55, 24]. In SBMI the representation of model prior could be further enhanced by lifting the restriction of an ordered model vector of fixed length. While this is conceptually tempting, the presented framework already covers many scientific scenarios. However, using more flexible embedding networks like transformer architectures [56, 57] could be used for this generalization and further generalize SBMI to simulator outputs  $x$  of varying size [42].

In summary, our method provides a powerful tool for data-driven scientific inquiry. It will allow scientists to systematically identify essential model components which are consistent with observed data. Incorporating the uncertainty into their model choices will help to resolve competing models and theories.

## Acknowledgments and Disclosure of Funding

We thank all group members of the Mackelab for their insightful discussions and valuable feedback on the manuscript. This work was funded by the Deutsche Forschungsgemeinschaft (DFG, German Research Foundation) under Germany’s Excellence Strategy – EXC number 2064/1 – 390727645, and under SFB 1233, Robust Vision: Inference Principles and Neural Mechanisms, project 6, number: 276693517 and by the German Federal Ministry of Education and Research (BMBF): Tübingen AI Center, FKZ: 01IS18039A.

## References

- [1] Nicolaus Copernicus. De revolutionibus orbium coelestium, 1543.
- [2] William Ogilvy Kermack and Anderson G McKendrick. A contribution to the mathematical theory of epidemics. *Proceedings of the royal society of london. Series A, Containing papers of a mathematical and physical character*, 115(772):700–721, 1927.
- [3] Herbert W Hethcote. The mathematics of infectious diseases. *SIAM review*, 42(4):599–653, 2000.
- [4] Alan L Hodgkin and Andrew F Huxley. A quantitative description of membrane current and its application to conduction and excitation in nerve. *The Journal of physiology*, 117(4):500, 1952.
- [5] David A McCormick and John R Huguenard. A model of the electrophysiological properties of thalamo-cortical relay neurons. *Journal of neurophysiology*, 68(4):1384–1400, 1992.
- [6] Martin Pospischil, Maria Toledo-Rodriguez, Cyril Monier, Zuzanna Piwkowska, Thierry Bal, Yves Frégnac, Henry Markram, and Alain Destexhe. Minimal hodgkin–huxley type models for different classes of cortical and thalamic neurons. *Biological cybernetics*, 99:427–441, 2008.
- [7] William F Podlaski, Alexander Seeholzer, Lukas N Groschner, Gero Miesenböck, Rajnish Ranjan, and Tim P Vogels. Mapping the function of neuronal ion channels in model and experiment. *Elife*, 6:e22152, 2017.
- [8] Roger Ratcliff. A theory of memory retrieval. *Psychological review*, 85(2):59, 1978.
- [9] Joshua I Gold and Michael N Shadlen. Representation of a perceptual decision in developing oculomotor commands. *Nature*, 404(6776):390–394, 2000.
- [10] Roger Ratcliff and Gail McKoon. The diffusion decision model: theory and data for two-choice decision tasks. *Neural computation*, 20(4):873–922, 2008.
- [11] Marius Usher and James L McClelland. The time course of perceptual choice: the leaky, competing accumulator model. *Psychological review*, 108(3):550, 2001.
- [12] Eric-Jan Wagenmakers, Han LJ Van Der Maas, and Raoul PPP Grasman. An ez-diffusion model for response time and accuracy. *Psychonomic bulletin & review*, 14(1):3–22, 2007.
- [13] Michael N Shadlen and Roozbeh Kiani. Decision making as a window on cognition. *Neuron*, 80(3):791–806, 2013.
- [14] Kenneth W Latimer, Jacob L Yates, Miriam LR Meister, Alexander C Huk, and Jonathan W Pillow. Single-trial spike trains in parietal cortex reveal discrete steps during decision-making. *Science*, 349(6244):184–187, 2015.
- [15] Brandon M Turner, Leendert Van Maanen, and Birte U Forstmann. Informing cognitive abstractions through neuroimaging: the neural drift diffusion model. *Psychological review*, 122(2):312, 2015.
- [16] Scott A Sisson, Yanan Fan, and Mark Beaumont. *Handbook of approximate Bayesian computation*. CRC Press, 2018.
- [17] George Papamakarios, Eric Nalisnick, Danilo Jimenez Rezende, Shakir Mohamed, and Balaji Lakshminarayanan. Normalizing flows for probabilistic modeling and inference. *Journal of Machine Learning Research*, 22(57):1–64, 2021.
- [18] Jan-Matthis Lueckmann, Pedro J Goncalves, Giacomo Bassetto, Kaan Öcal, Marcel Nonnenmacher, and Jakob H Macke. Flexible statistical inference for mechanistic models of neural dynamics. *Advances in neural information processing systems*, 30, 2017.

- [19] George Papamakarios and Iain Murray. Fast  $\epsilon$ -free inference of simulation models with bayesian conditional density estimation. *Advances in neural information processing systems*, 29, 2016.
- [20] Kyle Cranmer, Johann Brehmer, and Gilles Louppe. The frontier of simulation-based inference. *Proceedings of the National Academy of Sciences*, 117(48):30055–30062, 2020.
- [21] Maximilian Dax, Stephen R Green, Jonathan Gair, Michael Deistler, Bernhard Schölkopf, and Jakob H. Macke. Group equivariant neural posterior estimation. In *International Conference on Learning Representations*, 2022.
- [22] Norman Marlier, Olivier Bröls, and Gilles Louppe. Simulation-based bayesian inference for multi-fingered robotic grasping. *arXiv preprint arXiv:2109.14275*, 2021.
- [23] Pedro J Gonçalves, Jan-Matthis Lueckmann, Michael Deistler, Marcel Nonnenmacher, Kaan Öcal, Giacomo Bassetto, Chaitanya Chintaluri, William F Podlaski, Sara A Haddad, Tim P Vogels, et al. Training deep neural density estimators to identify mechanistic models of neural dynamics. *Elife*, 9:e56261, 2020.
- [24] Michael Deistler, Jakob H Macke, and Pedro J Gonçalves. Energy-efficient network activity from disparate circuit parameters. *Proceedings of the National Academy of Sciences*, 119(44):e2207632119, 2022.
- [25] Lukas N Groschner, Jonatan G Malis, Birte Zuidinga, and Alexander Borst. A biophysical account of multiplication by a single neuron. *Nature*, 603(7899):119–123, 2022.
- [26] Stefan T Radev, Ulf K Mertens, Andreas Voss, Lynton Ardizzone, and Ullrich Köthe. Bayesflow: Learning complex stochastic models with invertible neural networks. *IEEE transactions on neural networks and learning systems*, 33(4):1452–1466, 2020.
- [27] Jan Boelts, Jan-Matthis Lueckmann, Richard Gao, and Jakob H Macke. Flexible and efficient simulation-based inference for models of decision-making. *Elife*, 11:e77220, 2022.
- [28] Robert E Kass and Adrian E Raftery. Bayes factors. *Journal of the american statistical association*, 90(430):773–795, 1995.
- [29] Roberto Trotta. Bayes in the sky: Bayesian inference and model selection in cosmology. *Contemporary Physics*, 49(2):71–104, 2008.
- [30] A Spurio Mancini, MM Docherty, MA Price, and JD McEwen. Bayesian model comparison for simulation-based inference. *arXiv preprint arXiv:2207.04037*, 2022.
- [31] Jan Boelts, Jan-Matthis Lueckmann, Pedro J Goncalves, Henning Sprekeler, and Jakob H Macke. Comparing neural simulations by neural density estimation. In *Conference on Cognitive Computational Neuroscience*, pages 1289–1299, 2019.
- [32] Stefan T Radev, Marco D’Alessandro, Ulf K Mertens, Andreas Voss, Ullrich Köthe, and Paul-Christian Bürkner. Amortized bayesian model comparison with evidential deep learning. *IEEE Transactions on Neural Networks and Learning Systems*, 2021.
- [33] Michael Schmidt and Hod Lipson. Distilling free-form natural laws from experimental data. *science*, 324(5923):81–85, 2009.
- [34] Renáta Dubčáková. Eureka: software review, 2011.
- [35] Steven L Brunton, Joshua L Proctor, and J Nathan Kutz. Discovering governing equations from data by sparse identification of nonlinear dynamical systems. *Proceedings of the national academy of sciences*, 113(15):3932–3937, 2016.
- [36] Joseph Bakarji, Kathleen Champion, J Nathan Kutz, and Steven L Brunton. Discovering governing equations from partial measurements with deep delay autoencoders. *arXiv preprint arXiv:2201.05136*, 2022.
- [37] Miles Cranmer, Alvaro Sanchez Gonzalez, Peter Battaglia, Rui Xu, Kyle Cranmer, David Spergel, and Shirley Ho. Discovering symbolic models from deep learning with inductive biases. *Advances in Neural Information Processing Systems*, 33:17429–17442, 2020.
- [38] Georg Martius and Christoph H Lampert. Extrapolation and learning equations. *arXiv preprint arXiv:1610.02995*, 2016.

- [39] Subham Sahoo, Christoph Lampert, and Georg Martius. Learning equations for extrapolation and control. In Jennifer Dy and Andreas Krause, editors, *Proceedings of the 35th International Conference on Machine Learning*, volume 80 of *Proceedings of Machine Learning Research*, pages 4442–4450. PMLR, 10–15 Jul 2018.
- [40] Matthias Werner, Andrej Junginger, Philipp Hennig, and Georg Martius. Informed equation learning. *arXiv preprint arXiv:2105.06331*, 2021.
- [41] Matthias Werner, Andrej Junginger, Philipp Hennig, and Georg Martius. Uncertainty in equation learning. In *Proceedings of the Genetic and Evolutionary Computation Conference Companion*, pages 2298–2305, 2022.
- [42] Luca Biggio, Tommaso Bendinelli, Alexander Neitz, Aurelien Lucchi, and Giambattista Parascandolo. Neural symbolic regression that scales. In *International Conference on Machine Learning*, pages 936–945. PMLR, 2021.
- [43] Sören Becker, Michal Klein, Alexander Neitz, Giambattista Parascandolo, and Niki Kilbertus. Discovering ordinary differential equations that govern time-series. *arXiv preprint arXiv:2211.02830*, 2022.
- [44] Takashi Arai. Multivariate binary probability distribution in the grassmann formalism. *Physical Review E*, 103(6):062104, 2021.
- [45] Aaron Meurer, Christopher P Smith, Mateusz Paprocki, Ondřej Čertík, Sergey B Kirpichev, Matthew Rocklin, AMiT Kumar, Sergiu Ivanov, Jason K Moore, Sartaj Singh, et al. Sympy: symbolic computing in python. *PeerJ Computer Science*, 3:e103, 2017.
- [46] Maxwell Shinn, Norman H Lam, and John D Murray. A flexible framework for simulating and fitting generalized drift-diffusion models. *ELife*, 9:e56938, 2020.
- [47] Alvaro Tejero-Cantero, Jan Boelts, Michael Deistler, Jan-Matthis Lueckmann, Conor Durkan, Pedro J. Gonçalves, David S. Greenberg, and Jakob H. Macke. sbi: A toolkit for simulation-based inference. *Journal of Open Source Software*, 5(52):2505, 2020.
- [48] Mathieu Germain, Karol Gregor, Iain Murray, and Hugo Larochelle. Made: Masked autoencoder for distribution estimation. In *International conference on machine learning*, pages 881–889. PMLR, 2015.
- [49] Harold Jeffreys. *The theory of probability*. OUP Oxford, 1998.
- [50] Jeffrey Chan, Valerio Perrone, Jeffrey Spence, Paul Jenkins, Sara Mathieson, and Yun Song. A likelihood-free inference framework for population genetic data using exchangeable neural networks. *Advances in neural information processing systems*, 31, 2018.
- [51] Jamie D Roitman and Michael N Shadlen. Response of neurons in the lateral intraparietal area during a combined visual discrimination reaction time task. *Journal of neuroscience*, 22(21):9475–9489, 2002.
- [52] Jonas Beck, Michael Deistler, Yves Bernaerts, Jakob H Macke, and Philipp Berens. Efficient identification of informative features in simulation-based inference. *Advances in Neural Information Processing Systems*, 35:19260–19273, 2022.
- [53] David Zhao, Niccolò Dalmaso, Rafael Izbicki, and Ann B Lee. Diagnostics for conditional density models and bayesian inference algorithms. In *Uncertainty in Artificial Intelligence*, pages 1830–1840. PMLR, 2021.
- [54] Joeri Hermans, Arnaud Delaunoy, François Rozet, Antoine Wehenkel, and Gilles Louppe. Averting a crisis in simulation-based inference. *arXiv preprint arXiv:2110.06581*, 2021.
- [55] Jonathan Oesterle, Christian Behrens, Cornelius Schröder, Thoralf Hermann, Thomas Euler, Katrin Franke, Robert G Smith, Guenther Zeck, and Philipp Berens. Bayesian inference for biophysical neuron models enables stimulus optimization for retinal neuroprosthetics. *ELife*, 9:e54997, 2020.
- [56] Ashish Vaswani, Noam Shazeer, Niki Parmar, Jakob Uszkoreit, Llion Jones, Aidan N Gomez, Łukasz Kaiser, and Illia Polosukhin. Attention is all you need. *Advances in neural information processing systems*, 30, 2017.
- [57] Juho Lee, Yoonho Lee, Jungtaek Kim, Adam Kosiorek, Seungjin Choi, and Yee Whye Teh. Set transformer: A framework for attention-based permutation-invariant neural networks. In *International conference on machine learning*, pages 3744–3753. PMLR, 2019.

- [58] Adam Paszke, Sam Gross, Francisco Massa, Adam Lerer, James Bradbury, Gregory Chanan, Trevor Killeen, Zeming Lin, Natalia Gimelshein, Luca Antiga, et al. Pytorch: An imperative style, high-performance deep learning library. *Advances in neural information processing systems*, 32, 2019.
- [59] Aric A. Hagberg, Daniel A. Schult, and Pieter J. Swart. Exploring network structure, dynamics, and function using networkx. In Gaël Varoquaux, Travis Vaught, and Jarrod Millman, editors, *Proceedings of the 7th Python in Science Conference*, pages 11 – 15, Pasadena, CA USA, 2008.
- [60] Omry Yadan. Hydra - a framework for elegantly configuring complex applications. Github, 2019.
- [61] Takuya Akiba, Shotaro Sano, Toshihiko Yanase, Takeru Ohta, and Masanori Koyama. Optuna: A next-generation hyperparameter optimization framework. In *Proceedings of the 25th ACM SIGKDD International Conference on Knowledge Discovery and Data Mining*, 2019.

# Appendix

## A1 Software and Computational Ressources

All networks were implemented in *pytorch* [58]. Additionally, we used the following software and toolboxes in this work: *sbi* [47] for the implementation of SBMI, *NetworkX* [59] for the construction of prior graphs, *SymPy* [45] for symbolic calculations, *pyDDM* [46] as the backend for the DDM experiments. To manage the configuration settings we used *Hydra* [60] and the *Optuna Sweeper* [61] plugin for a coarse hyperparameter search in the DDM setting.

All models were trained on an Nvidia RTX 2080ti GPU accessed via a slurm cluster.

## A2 Mixture of Grassmann Distribution

Previously, Arai introduced the Grassmann formalism for multivariate binary distributions [44] by using anticommuting numbers, called Grassmann numbers. A Grassmann distribution  $\mathcal{G}$  is an  $n$ -dimensional binary distribution parameterized by an  $n \times n$  matrix  $\Sigma$ . The probability mass function of  $\mathcal{G}$  with parameter  $\Sigma$  on  $Y = (Y_1, \dots, Y_n)$  is defined as

$$\mathcal{G}(y|\Sigma) = \det \begin{pmatrix} \Sigma_{11}^{y_1}(1 - \Sigma_{11})^{1-y_1} & \Sigma_{12}(-1)^{1-y_2} & \dots \\ \Sigma_{21}(-1)^{1-y_1} & \Sigma_{22}^{y_2}(1 - \Sigma_{22})^{1-y_2} & \dots \\ \vdots & \vdots & \ddots \end{pmatrix}.$$

For a valid distribution  $\Sigma^{-1} - I$  must be a  $P_0$  matrix, but has otherwise no further constraints [44].

This definition gives access to the analytical derivations of properties such as the mean, covariance, and marginal and conditional distributions. Here, we only recapitulate the analytical formula for conditional distribution, which is used for sampling. Their derivation and further details can be found in [44]. In the following paragraph we follow the notation of Arai [44].

For a conditional distribution on  $Y = (Y_1, \dots, Y_n)$ , we denote by  $C$  the indices of the observed variables  $y_j \in \{0, 1\}$  and  $R$  the remaining indices  $R = \{1, \dots, n\} \setminus C$ . Without loss of generality, the parameter matrix can be written as

$$\Sigma = \begin{pmatrix} \Sigma_{RR} & \Sigma_{RC} \\ \Sigma_{CR} & \Sigma_{CC} \end{pmatrix}.$$

The conditional distribution is then given by the Grassmann distribution

$$p(y_R|y_C) = \mathcal{G}(y_R|\Sigma_{R|y_C})$$

with

$$\Sigma_{R|y_C} = \Sigma_{RR} - \Sigma_{RC}(\Sigma_{CC} - \text{diag}(1 - y_C))^{-1}\Sigma_{CR},$$

where  $\text{diag}(1 - y_C)$  is the diagonal matrix with  $(1 - y_C)$  on its diagonal. An analogous formula can be derived by using the notation  $\Lambda^{-1} = \Sigma$  [44].

**Mixture of Grassmann Distribution** We define a mixture of Grassmann distribution (MoGr) on  $\{0, 1\}^n$  in the same formalism as  $p(y) = \sum_i \alpha_i \mathcal{G}_i(y|\Sigma_i)$  for a finite partition  $\sum_i \alpha_i = 1$  and Grassmann distributions  $\mathcal{G}_i$ . Using the means  $\mu_i$  and covariances  $C_i$  for each component  $\mathcal{G}_i$  we can calculate the mean and covariance for the mixture distribution by introducing a discrete latent variable  $Z$  and reformulate the mixture distribution as

$$\begin{aligned} p(y|Z = i) &= \mathcal{G}_i(y|\Sigma_i), \\ p(Z = i) &= \alpha_i. \end{aligned}$$

Using the law of total expectation and variance we get analytical expressions for the mean and covariance of a MoGr:

$$\mathbb{E}[Y] = \mathbb{E}[\mathbb{E}[Y|Z = i]] = \sum_i \alpha_i \mu_i$$

and

$$\begin{aligned}\text{Cov}(Y) &= \mathbb{E}[\text{Cov}(Y|Z=i)] + \text{Cov}(\mathbb{E}[Y|Z=i]) \\ &= \sum_i \alpha_i C_i + \sum_i \alpha_i (\mu_i - \bar{\mu})(\mu_i - \bar{\mu})^T,\end{aligned}$$

where  $\bar{\mu} = \mathbb{E}[Y]$ .

To sample from a MoGr we use the standard procedure of first sampling one component  $z_i \sim p(Z)$ , and then using the conditional expression of a Grassmann distribution to sample  $y \sim \mathcal{G}_{z_i}$ .

**Implementation** Arai [44] proposed the following parametrization for  $\Sigma$  that ensures the  $P_0$  criterion for  $\Sigma$ :

$$\Sigma^{-1} = BC^{-1} + I,$$

where  $B$  and  $C$  are strictly row diagonal dominant matrices, namely

$$b_{ii} > \sum_{j \neq i} |b_{ij}|, \quad \text{and} \quad c_{ii} > \sum_{j \neq i} |c_{ij}|.$$

We make use of this parametrization by optimizing unconstrained matrices  $\tilde{B}$  and  $\tilde{C}$  and defining  $B$  by replacing the diagonal elements of  $\tilde{B}$  by

$$b_{ii} = \exp(\tilde{b}_{ii}) + \sum_{j \neq i} |\tilde{b}_{ij}|,$$

and analogously for  $C$ . Instead of  $\exp$  any other positive function could be chosen and even the non-negative ReLU function showed good training behaviour in initial experiments.

We used a similar parameterization for a mixture of Grassmann distribution for each component and a softmax layer to learn the partition  $\sum_i \alpha_i = 1$ .

## A3 Model Prior

**Sampling** To sample from the model prior, we perform a random walk on the prior graph. The walk starts at a defined start vertex and moves to the next vertex proportional to the weight of all outgoing edges. The walk continues until a maximal number of vertices are visited or until we reach an end vertex. We can encode additional prior knowledge by changing the edge weights dynamically during a walk. This allows us to favor simple models or to dis- or encourage the co-occurrence of specific model components.

## A4 Inference

### A4.1 Model Posterior Network

We used a conditional MoGr distribution as model posterior network. The conditional parameters  $\Sigma_i|x$  are parameterized by two matrices  $B_i$  and  $C_i$  (Section A2). We used a fully connected neural network with ReLU activation to parametrize the unconstrained matrices  $\tilde{B}_i$ ,  $\tilde{C}_i$  and a softmax layer for the partition  $\alpha$  with  $\sum_i \alpha_i = 1$ . The input to the MoGr network is the output  $e(x)$  of the embedding net and the used hyperparameters can be found in Table S2 and S4.

### A4.2 Parameter Posterior Network

For the parameter posterior network, we used a conditioned mixture of (Gaussian) density network, which allowed us to marginalize analytically over the parameters of the absent model components during training time. For efficient training, we divided each batch into sub-batches with the same number of parameters and processed each sub-batch in parallel.

The conditioning network was implemented as fully connected network with ReLU activation. The specifics for the two settings can be found in Table S2 and S4.

---

**Algorithm 1:** Simulation-base model inference: SBMI

---

**Inputs:** Model prior  $p(M)$ , parameter priors  $p(\theta|M)$ , compiler  $C$ , number of simulations  $L$ , embedding net  $e_\zeta(x)$ , model posterior network  $q_\psi(M|e)$ , parameter posterior network  $q_\phi(\theta|M, e)$ .

**Outputs:** Trained embedding network  $e_\zeta(x)$ , model posterior network  $q_\psi(M|x)$ , parameter posterior network  $q_\phi(\theta|M, x)$ .

**Generate dataset:**

```
for  $l = 1, \dots, L$  do
     $M_l \sim p(M)$  ; # sample model
     $\theta_l \sim p(\theta|M_l)$  ; # sample parameters
     $S_l \leftarrow C(M_l, \theta_l)$  ; # compile simulator
     $x_l \sim S_l$  ; # simulate data
return  $\{(M_l, \theta_l, x_l)\}_{l=1, \dots, L}$ 
```

**Training:** ; # We omit the use of training batches here.

```
while not converged do
     $\mathcal{L}^M \leftarrow -\frac{1}{L} \sum_l \log q_\psi(M_l|e_\zeta(x_l))$  ; # compute model loss
     $\mathcal{L}^\theta \leftarrow -\frac{1}{L} \sum_l \log q_\phi(\theta_l|M_l, e_\zeta(x_l))$  ; # compute parameter loss
     $(\zeta, \psi, \phi) \leftarrow (\zeta, \psi, \phi) - \text{Adam}(\nabla_{(\zeta, \psi, \phi)}(\mathcal{L}^M + \mathcal{L}^\theta))$  ; # take gradient step
return  $e_\zeta(x), q_\psi(M|x), q_\phi(\theta|M, x)$ 
```

---

### A4.3 Training

We used the standard training loop of the *sbi* toolbox [47]: as validation set, we used 10% of the training samples and as stopping criterion we defined 25 consecutive epochs of no improvement of the loss function on the validation set.

For the additive model we used a batch size of 3000 samples, for the DDM a batchsize of 2000 samples.

## A5 Performance Measures

### A5.1 MAP Estimate

Once we trained the full network, we can easily get a *maximum a posteriori* estimate (MAP) by searching the discrete model space:

$$\begin{aligned} \max_{M, \theta} p(M, \theta|x_o) &= \max_{M, \theta} p(M|x_o) \cdot p(\theta|M, x_o) \\ &= \max_{i \in I} \{p(M_i|x_o) \cdot \max_{\theta} p(\theta|M_i, x_o)\}. \end{aligned}$$

While mathematically correct, this MAP is often dominated by the density function of the parameter posterior, which can take arbitrarily large values for small variances and can be susceptible to noise in the training process. The discrete distribution  $p(M|x_o)$  is, however, bounded in  $[0, 1]$ . Therefore, we are often interested in the more stable MAP parameter estimates of the most likely model:

$$\theta_{map} = \underset{\theta}{\operatorname{argmax}} p(\theta|M_{map}, x_o),$$

where  $M_{map} = \underset{M_i, i \in I}{\operatorname{argmax}} p(M_i|x_o)$ .

This MAP of the most likely model is shown as  $f_{MAP}$  in Figure 3d.

### A5.2 Additive Model

For the additive model we can approximate the ground truth model posterior  $p(M|x_o)$  by calculating the model evidence by

$$p(M|x_o) = \frac{p(x_o|M)p(M)}{p(x_o)} \sim p(x_o|M)p(M).$$



The prior  $p(M)$  is only given implicitly, but as the model space is low-dimensional, we can approximate the prior by the empirical sampling distribution  $\hat{p}(M)$  (shown in Fig. 3). We therefore get the approximation

$$\begin{aligned} p(M|x_o) &\sim p(M) \int p(x_o|M, \theta) p(\theta|M) d\theta \\ &\approx \hat{p}(M) \frac{1}{N} \sum_{j=1}^N p(x_o|M, \theta_j), \end{aligned}$$

where  $\theta_j$  are samples from the parameter prior  $p(\theta|M)$ . Since we used a Gaussian noise model, we can calculate the expression  $p(x_o|M, \theta_j)$  by evaluating  $\mathcal{N}(f_{\theta_j}(t), \Sigma_{\theta_j}(t))$ .

In practice, we apply importance sampling to avoid regions with a low probability, such that we get

$$p(M|x_o) \sim \hat{p}(M) \frac{1}{N} \sum_{j=1}^N p(x_o|M, \theta_j) \frac{p(\theta_j|M)}{q_\phi(\theta_j|M, x_o)},$$

where  $\theta_j \sim q_\phi(\theta|M, x_o)$  are samples from the approximated parameter posterior.

Even with importance sampling, a lot of samples were necessary to get reliable estimates. We used 100k samples  $\theta_j \sim q_\phi(\theta|M, x_o)$  per observation and were therefore restricted to few observations  $x_o$  (100 for the presented results in Section 3.1).

### A5.3 DDM

We used the mean-squared error (MSE) on the weighted density functions of the two different decisions, similar to [46]. In the same work, they showed that the relative MSE is in good correspondence with other performance metrics on the used experimental data. We therefore used the loss function implemented as `LossSquaredError` in the *pyDDM* package [46].

## A6 Model Details

### A6.1 Additive Model

Table S1: **Details for the additive model.** The parameter  $\theta_1$  in the noise terms  $n_1$  and  $n_2$  defines the standard deviation of a normal distribution  $\mathcal{N}$ , and  $\mathcal{U}(a, b)$  defines a uniform distribution on the interval  $[a, b]$ . For the performance we report the mean and standard deviation.

Model Component	Token	Parameter Prior	Performance $\hat{p}_{\text{reference}}(M_i x_o)$	Performance $q_\psi(M_i x_o)$
$\theta_1 \cdot t$	$l_1$	$\theta_1 \sim \mathcal{U}(-2, 2)$	0.70 (0.27)	0.65 (0.24)
$\theta_1 \cdot t^2$	$l_2$	$\theta_1 \sim \mathcal{U}(-2, 2)$	0.70 (0.26)	0.67 (0.24)
$\theta_1 \cdot t^2$	$q$	$\theta_1 \sim \mathcal{U}(-0.5, 0.5)$	0.97 (0.09)	0.93 (0.15)
$\theta_1 \cdot \sin(\theta_2 t)$	$\sin$	$\theta_1 \sim \mathcal{U}(0, 5)$ $\theta_2 \sim \mathcal{U}(0.5, 5)$	0.95 (0.15)	0.91 (0.18)
noise <sub>1</sub> : $n_{t_i} \sim \mathcal{N}(0, \theta_1)$	$n_1$	$\theta_1 \sim \mathcal{U}(0.1, 2)$	1.00 (0.00)	1.00 (0.00)
noise <sub>2</sub> : $n_{t_i} \sim (t_i + 1)\mathcal{N}(0, \theta_1)$	$n_2$	$\theta_1 \sim \mathcal{U}(0.5, 2)$	1.00 (0.00)	1.00 (0.00)

**Prior** To show the flexibility of the presented prior over model components, we defined a dynamically changing graph for the additive model. During a random walk, we increased the edge weights of the direct model paths to the end node with every sampled component and additionally decreased the weight between the linear components if one component is sampled by a factor of two. This favors simple models and disadvantages the co-occurrence of both linear components. The resulting empirical prior distribution is shown in grey in Figure 3b.

The parameter priors for the model components are shown in Table S1.

**Network Details** We used a one-dimensional convolutional network followed by fully connected layers as an embedding net for the additive model. The convolutional layers used a kernel size of five and stride one. The output of the last convolutional layer was flattened before passing it on to the fully connected network. All further parameters can be found in Table S2.

Table S2: **Network details for the additive model.** Square brackets indicate the layer-wise parameters, otherwise the same parameters were used for all layers.

	Number of Layers	Dimensions / #Channels	Components
Convolutional layers	2	[10, 16]	-
Fully connected layers	3	[200, 200, 50]	-
MoGr net	3	80	3
MDN net	3	120	3

## A6.2 DDM

Drift diffusion models can be described as a stochastic differential equation for a decision variable  $z$ :

$$dz = d(z, t)dt + dW,$$

with initial condition  $z_0$ , drift term  $d$ , and a Wiener noise process  $W$ . A decision is taken when the decision variable hits the boundary  $|d(z, t)| \geq b(t)$  (Figure 4a). An additional parameter delays the starting time of the process (‘non-decision time’).

We included two different drift terms  $d$ :

1. constant drift:  $d(z, t) = \theta_1$ , and
2. leaky drift:  $d(z, t) = \theta_1 + \theta_2 \cdot z$  (with  $\theta_2 < 0$ ),

and two boundary conditions  $b$ :

1. constant boundary:  $b(t) = \theta_1$ , and
2. exponentially collapsing boundary:  $b(t) = \theta_1 - \exp(-t/\theta_2)$ .

The initial condition  $z_0$  was fixed to be zero and the noise term had a constant standard deviation of one. The non-decision time was a free parameter but was present in all models (see Figure 4b).

Table S3: **Details for the DDM.** We used independent uniform distributions  $\mathcal{U}$  for all parameter priors. The performances were calculated on 1k samples from the prior distribution, and we report mean and standard deviation.

Model Component	Token	Parameter Prior	Performance Model Posterior	Performance Model MAP
constant drift	$d_c$	$\theta_1 \sim \mathcal{U}(0, 5)$	0.85 (0.23)	0.90 (0.31)
leaky drift	$d_l$	$\theta_1 \sim \mathcal{U}(0, 5)$ $\theta_2 \sim \mathcal{U}(-20, -5)$	0.85 (0.23)	0.90 (0.31)
constant boundary	$b_c$	$\theta_1 \sim \mathcal{U}(0.3, 2)$	0.90 (0.20)	0.92 (0.27)
exp. collapsing boundary	$b_{exp}$	$\theta_1 \sim \mathcal{U}(0.3, 2)$ $\theta_2 \sim \mathcal{U}(0.5, 1.5)$	0.90 (0.20)	0.92 (0.27)
non-decision time	$ndt$	$\theta_1 \sim \mathcal{U}(0.1, 0.3)$	1.00 (0.00)	1.00 (0.00)

**Training Data** We used the *pyDDM* toolbox [46] to solve the DDM numerically for every  $\theta$  using the Fokker-Planck equation. From the approximated decision time and choice distribution we then sampled 400 iid trials for each  $\theta$ . This results in a  $400 \times 2$  data matrix with the recorded continuous decision times and binary decisions.

As training data, we sampled 200k models from the prior, solved these DDMs and drew 400 trials. From this data, we excluded datapoints with more than 300 undecided trials (defined as trials with a decision time larger than 10 seconds). From the remaining  $\approx 180$ k datapoints we hold back 1k test datapoints and divided the other part into 10% validation and 90% training data.

**Prior** All edges of the model prior have the same initial weight in the shown prior graph (Figure 4b). If the leaky drift component is visited in a random walk, the edge weight of the constant boundary condition is decreased by a factor of two.

The parameter priors for the different model components are shown in Table S3

**Network Details** To account for the iid trial structure of the DDM data, we used a permutation invariant embedding net [50, 26]. Each trial (represented as a vector (decision time, decision)) is first processed by the ‘single trial net’, which we implemented as a fully connected neural network. The output is then averaged (making it permutation invariant) and passed on to a second fully connected network. The used hyperparameters (Table S4) were the best hyperparameters in a coarse hyperparameter sweep over eight models, varying three hyperparameters. To this end, we used *Optuna* [61] and varied the embedding dimensions (last layer of the single trial net and the last layer of the fully connected embedding net) and the dimension of the MoGr net.

Table S4: **Network details for the DDM.** Square brackets indicate the layer-wise parameters, otherwise the same parameters were used for all layers.

	Number of Layers	Dimensions	Components
Single trial net	3	[120, 120, 100]	-
Fully connected embedding net	3	[120, 120, 30]	-
MoGr net	3	80	3
MDN net	3	120	3

**Dataset** The used data [51] was collected from two monkeys performing a random dot motion discrimination task. Visual stimuli of moving dots with different coherence rates (0, 3.2, 6.4 and 12.8%) were presented and the monkeys had to decide on the moving direction. We randomly subsampled 400 trials for each stimulus condition to match the dimension of our training data and show the results for ‘monkey N’ throughout the manuscript. The dataset can be found here: <https://shadlenlab.columbia.edu/resources/RoitmanDataCode.html>.

Table S5: **DDM parameter comparison for example observation.** Sample mean and standard deviation for 10k samples from the SBMI parameter posterior for the example observation from Figure 4. The model posteriors are  $q_\psi(\text{gt-model}|x_o) = 0.75$  and  $q_\psi(\text{c.-drift-model}|x_o) = 0.25$ .

Model Component	Parameter	Ground Truth	SBMI posterior   gt-model	SBMI posterior   c.-drift-model
constant drift	$\theta_1$	-	-	1.37 (0.08)
leaky drift	$\theta_1$	2.00	1.79 (0.17)	-
	$\theta_2$	-10.00	-9.71 (3.60)	-
constant boundary	$\theta_1$	-	-	-
exp. collapsing boundary	$\theta_1$	0.70	0.75 (0.13)	1.73 (0.15)
	$\theta_2$	0.70	0.76 (0.11)	1.07 (0.11)
non-decision time	$\theta_1$	0.25	0.22 (0.03)	0.14 (0.02)

Table S6: **DDM predictive performance for experimental data.** Comparison of mean decision times  $\mu$  and standard deviation of decision times  $\sigma$  of the experimental data ( $\hat{\cdot}$ ) to posterior predictive samples. We report the mean and standard deviation for the different measures based on 10k SBMI posterior samples and for ten *pyDDM* fits with different random seeds. The statistics are pooled over the different coherence rates.

Measure	<i>pyDDM</i>	SBMI
decision time: $ \mu - \hat{\mu} $	0.06 (0.06)	0.06 (0.06)
decision time: $ \sigma - \hat{\sigma} $	0.17 (0.15)	0.13 (0.15)
deviation correct trials in %	2.08 (1.75)	2.22 (1.83)
MSE on densities ( $\cdot 10^{-2}$ )	9.66 (9.18)	9.66 (8.94)

## A7 Supplementary Figures

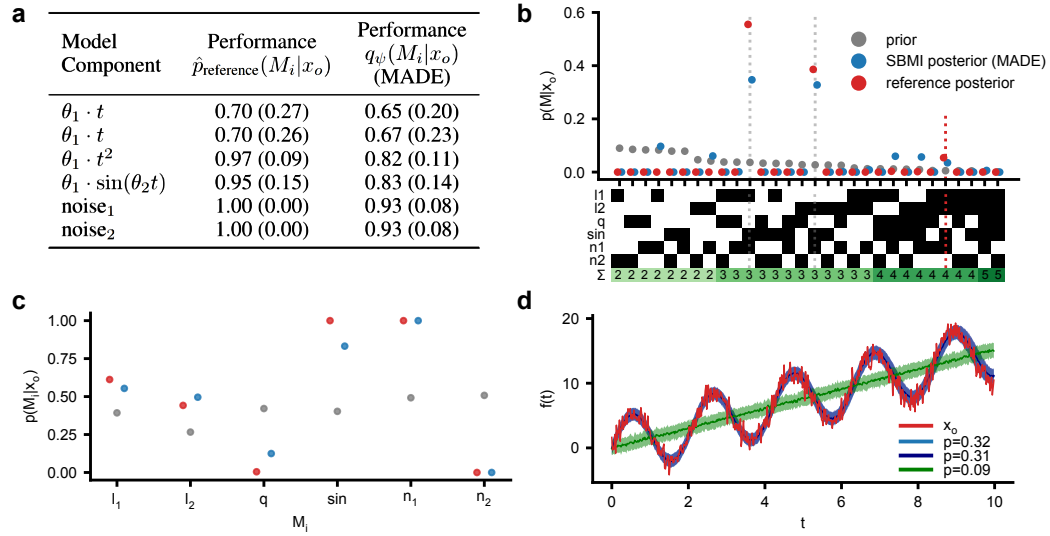


Figure S1: **SBMI on the Additive Model** (using MADE instead of MoGr). **(a)** Table with marginal posterior performance for the different model components of the additive model. Initial experiments showed a worse performance of the posterior implemented as MADE compared to a MoGr (Table S1). **(b)** Model posterior implemented as MADE conditioned on  $x_o$  shown in (d) (similar to Fig. 3b). **(c)** Marginal model posterior implemented as MADE for the same observation. **(d)** Posterior predictives (and local uncertainties as mean  $\pm$  std.) of the three most likely models, covering 72% of the model posterior mass. Compared to Fig. 3d models without the sinusoidal get non-negligible posterior mass.

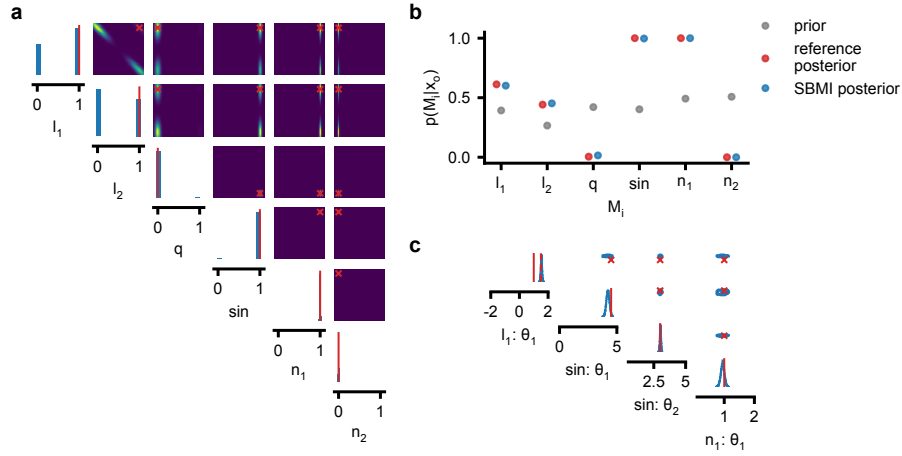


Figure S2: **SBMI posterior for the additive model.** (a) Smoothed one- and two-dimensional marginal distribution for the (binary) model posterior. The ground truth model is indicated in red. (b) Marginal model posterior distribution for the observation  $x_o$  shown in Figure 3. The ground truth model consists of the components  $l_1$ ,  $l_2$ ,  $\sin$ , and  $n_1$ . (c) One- and two-dimensional marginal distribution of the SBMI parameter posterior given the MAP model. The ground truth parameters are indicated in red. The sum of the coefficients  $\theta_1$  for the two linear components  $l_1$  and  $l_2$  of the ground truth model is indicated as a dashed line in the most left plot. It matches the mean of the posterior marginal for  $l_1$ .

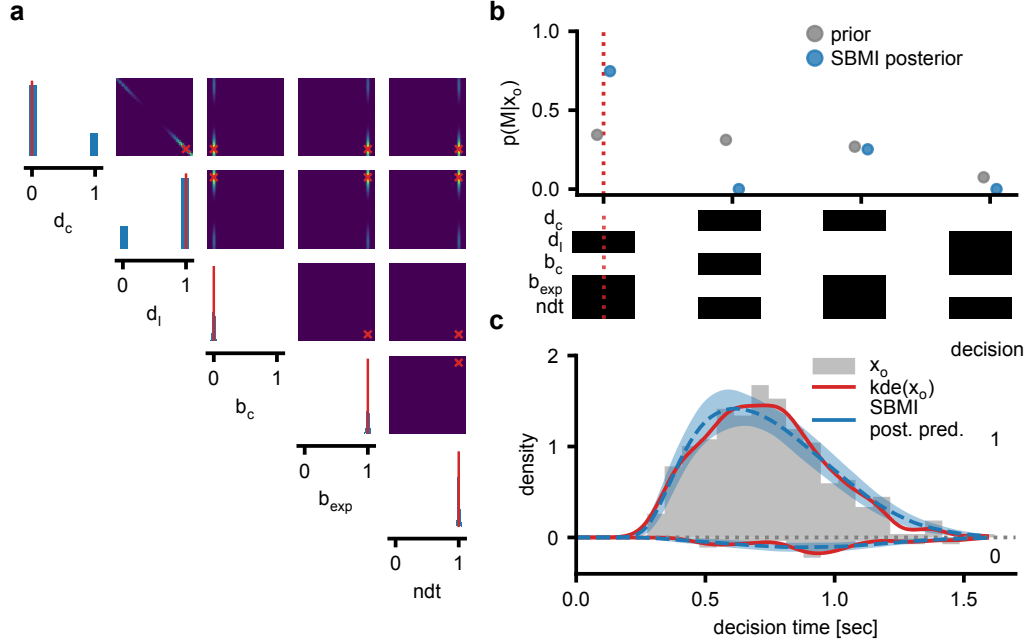


Figure S3: **DDM posterior and posterior predictives.** (a) Smoothed one- and two-dimensional marginal distribution for the (binary) model posterior. The ground truth model is indicated in red. (b) Model prior and SBMI model posterior with the ground truth model indicated as a red dotted line. (c) Posterior predictives for the example observation of Figure 4. The global uncertainty is shown as mean  $\pm$  std. over predictions from different model posterior samples.

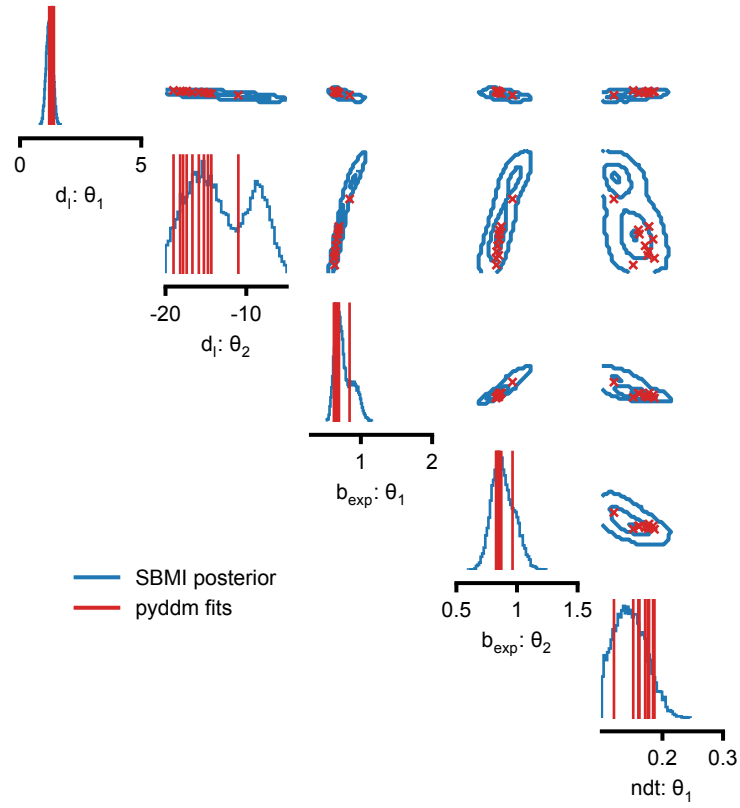


Figure S4: **Parameter posterior distribution for the DDM on experimental data.** One- and two-dimensional marginals of the SBMI parameter posterior for a coherence rate of 6.4%. Red markers indicate ten *pyDDM* fits for a fixed model with different random seeds, all resulting in similar loss values.